bioRxiv preprint doi: https://doi.org/10.1101/105569; this version posted March 2, 2017. The copyright holder for this preprint (which was not certified by peer review) is the author/funder. All rights reserved. No reuse allowed without permission.

microCT-Based Skeletal Phenomics in Zebrafish Reveals Virtues of Deep Phenotyping at the Whole-Organism Scale

Short Title: Skeletal Phenomics in Zebrafish

Matthew Hur[1], Charlotte A. Gistelinck[2], Philippe Huber[1], Jane Lee[1], Marjorie H. Thompson[1], Adrian T. Monstad-Rios[1], Claire J. Watson[1], Sarah K. McMenamin[3], Andy Willaert[2], David M Parichy[4], Paul Coucke[2], Ronald Y. Kwon[1,5]

[1] Department of Orthopaedics and Sports Medicine, University of Washington, Seattle, Washington, USA

[2] Center for Medical Genetics, Ghent University, Ghent, Belgium

[3] Biology Department, Boston College, Chestnut Hill, Massachusetts, USA

[4] Department of Biology, University of Virginia, Charlottesville, VA, USA

[5] Corresponding author: ronkwon@uw.edu

bioRxiv preprint doi: https://doi.org/10.1101/105569; this version posted March 2, 2017. The copyright holder for this preprint (which was not certified by peer review) is the author/funder. All rights reserved. No reuse allowed without permission.

ABSTRACT

Phenomics -- in-depth phenotyping at the whole-organism scale -- holds promise to significantly enhance our functional understanding of genes and genomic variation, yet methods in vertebrates are limited. Here, we demonstrate rapid whole-body profiling of hundreds of traits in the axial skeleton of adult zebrafish. We show the potential for vertebral patterns to confer heightened sensitivity, with similar specificity, in discriminating mutant populations compared to analyzing individual vertebrae in isolation, even when the latter is performed at higher resolution. We identify phenotypes associated with human brittle bone disease and thyroid stimulating hormone receptor hyperactivity. Finally, we develop allometric models and show their potential to discriminate mutant phenotypes masked by growth alterations in growth. Our studies demonstrate virtues of deep phenotyping in a single organ system. Phenomic pattern analysis may increase productivity in genetic screens, and facilitate the study genetic variants of smaller effect size, such as those that underlie complex diseases.

bioRxiv preprint doi: https://doi.org/10.1101/105569; this version posted March 2, 2017. The copyright holder for this preprint (which was not certified by peer review) is the author/funder. All rights reserved. No reuse allowed without permission.

INTRODUCTION

Advances in genomic sequencing have revolutionized our ability to identify genes and genetic variations important for health, yet our ability to characterize vertebrate phenomes – i.e., to acquire in-depth phenotypic profiles at the scale of the whole organism [1] – remains limited. The development of vertebrate phenotypic assays that approach the scale and efficiency of genomic technologies hold promise to fundamentally enhance our functional understanding of genes and genomic variation. For instance, they could rapidly accelerate genetic and drug discovery by enabling organism-wide, unbiased analysis of a large number of traits. In addition, they could expand our understanding of functional relationships between genes by enabling the clustering of gene mutations into common pathways based on similarities in phenotypic signatures. Finally, there are likely to be benefits of phenomic profiling that are difficult to anticipate [1]. Specifically, since our functional understanding of genes and genomic variation is directly coupled to the depth in which we are able to characterize their effects on phenotype, our understanding of gene function is fundamentally limited by the tendency for phenotypic assays to be restricted to a few readouts [1-3]. A better understanding of the biological insights that may be attained by profiling changes in patterns in a large number of traits is essential to both guide and drive the development of next-generation phenotyping technologies.

As an organ system consisting of a large number of tissues distributed throughout the body, the skeleton is a prime example of a biological system that may benefit from phenomic approaches. The skeleton comprises bones of different developmental origins (i.e., intramembranous vs. endochondral ossification), cellular compositions, and gene expression patterns. Different compartments can be differentially regulated through differences in local mechanical environment, proximity to tissues/organs that exert paracrine control (e.g., at the muscle/bone interface), and

bioRxiv preprint doi: https://doi.org/10.1101/105569; this version posted March 2, 2017. The copyright holder for this preprint (which was not certified by peer review) is the author/funder. All rights reserved. No reuse allowed without permission.

variations in vascularization and innervation. Since different gene mutations often affect different skeletal compartments, it is common practice to perform skeletal phenotyping at multiple skeletal sites. However, most efforts to increase the phenotypic content of skeletal assays have focused on increasing the intensity of phenotyping at a given anatomical location rather than increasing the number of bones/compartments analyzed. In mice, Adams et al. [4] developed a semi-automated workflow integrating microCT and multi-image cryohistology [5, 6] to quantify 15 traits in the femur and lumbar spine. Using a high-throughput automated synchrotron-based tomographic microscopy system, Mader et al. [7] quantified 22 different traits in the mouse femur. In zebrafish, Pardo-Martin et al. [8] used automated sample handling and optical projection tomography to acquire high-dimensional phenotypic profiles (~200 traits) in the craniofacial cartilage of early larvae, representing one of the most ambitious approaches to perform large-scale phenotyping in the skeleton to date. Yet, even in this analysis, traits were derived from only 9 skeletal elements. Further, this method is not readily extendable to bones outside of the craniofacial skeleton, or to adults. Finally, while both the mouse and zebrafish spine are amenable to whole-body microCT imaging [9, 10], in-depth phenotyping is usually limited to a few vertebral bodies [11]. In this context, methods to profile and analyze a large number of bones from whole-body datasets represents a unique class of problems that has not been adequately addressed.

Here, we present microCT-based methods and a new segmentation algorithm, FishCuT, enabling rapid (<5min/fish), whole-body profiling of hundreds of morphological and densitometric traits in the axial skeleton of adult zebrafish. We developed a statistical workflow to test for differences in phenomic patterns in mutant populations, and show through multiple analytical strategies the potential for vertebral patterns to confer heightened sensitivity, with similar specificity, in discriminating mutant populations compared to analyzing individual vertebrae in isolation, even when the latter is

bioRxiv preprint doi: https://doi.org/10.1101/105569; this version posted March 2, 2017. The copyright holder for this preprint (which was not certified by peer review) is the author/funder. All rights reserved. No reuse allowed without permission.

performed at higher resolution. We performed in-depth phenotyping in zebrafish models of brittle bone disease and thyroid stimulating hormone receptor (*tshr*) hyperactivity, and identify multivariate phenotypes in zebrafish associated with human skeletal disease. Finally, we developed phenome-based allometric models and show that they are able to discriminate mutant phenotypes masked by alterations in growth. We have integrated our methods into a software package, FishCuT, whose source code has been deposited on GitHub as a beta release (https://github.com/ronaldkwon/FishCuT).

RESULTS

A microCT-Based WorkFlow For Rapid Phenomic Profiling in Adult Zebrafish

Due to their small size, zebrafish are conducive to whole-body microCT imaging at high resolution [12]. Previous studies have demonstrated radiopacity in adult zebrafish vertebrae [13] and the viability of imaging vertebral morphology in adult zebrafish via microCT [9, 10, 14-16]. In our studies, we found that the small size of zebrafish can be exploited by imaging multiple fish simultaneously. For instance, we routinely image two fish at a time (enabling acquisition of whole body scans at 21µm resolution in ~20min/fish), and have found that up to eight animals can be scanned simultaneously at 21µm resolution, resulting in an effective scan time of ~5min/fish. In this context, the primary bottleneck to whole-body skeletal analysis is not the time required for microCT scan acquisition, but the time required for segmenting large microCT datasets. As an example, we found that ~60min was required to manually segment a single vertebra of an adult fish scanned at 21µm resolution (~60 image slices) using a user-assisted segmentation tool, a rate that would require >24hrs to segment the ~27 precaudal and caudal vertebrae that comprise the zebrafish vertebral column.

bioRxiv preprint doi: https://doi.org/10.1101/105569; this version posted March 2, 2017. The copyright holder for this preprint (which was not certified by peer review) is the author/funder. All rights reserved. No reuse allowed without permission.

To overcome this barrier, we developed FishCuT, a microCT analysis toolkit that couples supervised segmentation with connectivity analysis to enable rapid computation of hundreds of descriptors of bone morphology, mass, and mineralization in the vertebral column of adult zebrafish (Fig 1). To segment vertebral bodies, FishCuT employs a region-growing algorithm which takes user-specified line regions of interest (ROIs) specifying "seed" locations of vertebral boundaries, and uses them to isolate individual vertebrae. This segmentation is achieved by iteratively growing a separation boundary such that each vertebra is composed of connected components that do not contain voxels from different vertebrae. Once each vertebral body is segmented (Fig 1B), a supervised algorithm is used to segment each vertebral body into three skeletal elements: the neural arch (Neur), centrum (Cent), and haemal arch/ribs (Haem) (Fig 1C). For each skeletal element, four primary parameters are computed: Tissue Mineral Density (TMD, mgHA/cm^3), Volume (Vol, µm^3), Thickness (Th, µm), and Surface Area (SA, µm^2) (Fig 1D). In addition to the above traits, FishCuT computes centrum length (Cent.Le, µm), as well as intra-specimen variation in TMD and thickness (i.e. TMD.sd and Th.sd, respectively [11, 17]) for each skeletal element. For each trait, the "total" value (e.g., Tot.TMD) within a single vertebra (i.e., across the centrum, haemal arch/ribs, and neural arch) is also computed. For analysis, we developed a statistical testing procedure where each combination of element/outcome (e.g., Cent.TMD) is computed as a function of vertebra number, and the global test [18, 19], a regression-based statistical test designed for data sets in which many covariates (or features) have been measured for the same subjects, is used to assess whether the pattern across vertebrae is significantly different between groups. This output is provided graphically via a custom R script that computes plots of phenotypic trends (Fig 1E), and color codes them to highlight which trends are statistically significant in the global test. Finally, for each combination of outcome/element, a standard score is computed as the difference between its value in each vertebral body and its mean value across all vertebrae in the

bioRxiv preprint doi: https://doi.org/10.1101/105569; this version posted March 2, 2017. The copyright holder for this preprint (which was not certified by peer review) is the author/funder. All rights reserved. No reuse allowed without permission.

control population, divided by the standard deviation across all vertebrae in the control population. These data are arranged into matrix constructs that we have termed "skeletal barcodes". These data can be input into graphing software to generate heat maps to facilitate visualization of phenotypic trends both within individuals and across groups (Fig 1F). Using this process, we are able to segment 24 vertebrae into 72 different skeletal compartments to quantify ~600 different traits, with image analysis usually taking <5min/fish (~100x faster than manual segmentation).

To assess segmentation quality, we analyzed a single wildtype zebrafish (strain, AB; standard length, S.L.: 24.8mm) using two different approaches -- FishCuT and manual segmentation -- and used the Dice similarity coefficient (DSC) [20] to evaluate spatial overlap in segmentations produced by the two approaches. We computed a DSC of 0.932±0.001 (mean±SD, n=2 vertebrae) when we excluded pixels with intensities less than the threshold used in the FishCuT analysis, exceeding the value of 0.7 suggested to indicate excellent agreement between manual and automated segmentation approaches [21]. We computed a mean difference of 3.4±1.2% (mean±SD, n=3 fish) in centrum length, a measure that is calculated directly from user-specified "seed" locations of the vertebral boundaries, when we serially performed primary and secondary scans of the same animal. This suggests that intra-operator reproducibility during this step was high. Finally, to assess independence among traits, we computed Pearson correlation coefficients for each pair of traits across all 34 fish analyzed in this study. We observed a relatively low median absolute Pearson correlation coefficient of 0.34 among traits (Fig 2, Fig 2-Source Data 1), similar to the value of 0.3 attained by Pardo-Martin et al. during high-content profiling of the zebrafish craniofacial skeleton [8]. This quantity was relatively invariant with increasing number of vertebrae used for analysis (Fig 2-Figure Supplement 1), consistent with the notion that each vertebra confers non-redundant information.

bioRxiv preprint doi: https://doi.org/10.1101/105569; this version posted March 2, 2017. The copyright holder for this preprint (which was not certified by peer review) is the author/funder. All rights reserved. No reuse allowed without permission.

MicroCT Imaging at Medium and High Resolution Exhibit Comparable Ability to Distinguish Mutant Phenotypes

Due to the large volumes that must be analyzed, whole-body phenomics requires a balance between image resolution and throughput. We assessed a) the correlation in traits quantified using scans performed at 21µm (medium) vs. 10.5µm (high) nominal resolution, and b) the sensitivity of these two resolutions in discriminating mutant phenotypes in known skeletal mutants. For testing, we used *bmp1a*$^{-/-}$ mutant fish. In humans, mutations in *BMP1* result in a rare recessive form of the brittle bone disease Osteogenesis Imperfecta (OI) [22]. In zebrafish, the *frilly fins* (*frf*) mutant harbors mutations in *bmp1a* [15] and exhibits high vertebral bone mineral density (BMD) in adults, mimicking the high BMD phenotype in humans with OI caused by *BMP1* mutations [22]. We serially scanned n=3 *bmp1a*$^{-/-}$ mutant fish and WT sibling controls (S.L. of WT: 25.7±1.2mm, S.L. of mutant: 23.2±1.0mm, mean±SD, S.L.=standard length) at medium and high resolutions, analyzed scans using FishCuT, and compared quantities from individual vertebrae via linear regressions (Fig 3, Fig 3-Source Data 1). In general, we observed extremely high correlations between values attained at the two scanning resolutions, with R^2 values ranging from 0.98 to >0.99. In most cases, slopes deviated slightly from unity: slopes ranged from 0.90 to 0.91 for TMD measurements, while it ranged 1.18 to 1.21 for thickness measurements (we did not observe a consistent trend for volumetric measurements). This deviation from unity is likely to due to partial volume effects (PVEs; an inherent property of microCT images that emerges from projecting a continuous object onto a discrete grid [23]). However, due to the high correlation in measurements attained at each resolution, we observed minimal impact of PVEs on sensitivity in discriminating mutant phenotypes, as t-tests for differences in single vertebrae between WT and *bmp1a*$^{-/-}$ fish yielded similar p-values regardless of scan resolution used (see Fig 3 for values). Collectively, these analyses suggest that

bioRxiv preprint doi: https://doi.org/10.1101/105569; this version posted March 2, 2017. The copyright holder for this preprint (which was not certified by peer review) is the author/funder. All rights reserved. No reuse allowed without permission.

microCT scans at high and medium resolutions provided highly correlated information on each trait, and were comparable in their ability to discriminate WT from mutant phenotypes.

Phenomic Profiling Enhances Sensitivity in Discriminating Mutant Populations

As described above, for statistical testing we developed a procedure whereby each combination of element/outcome is computed as a function of vertebra number, and the global test is used to assess whether the pattern across vertebrae is significantly different between groups. We hypothesized that phenomic profiling, in concert with the global test, may provide greater sensitivity in distinguishing mutant populations compared to a) t-tests of individual vertebrae, and b) t-tests of quantities averaged across all vertebrae.

To test this, we used the n=3 WT and *bmp1a*$^{-/-}$ fish from the previous section to estimate means and covariances for each trait in each population and used them to construct distributions for Monte Carlo simulations (10,000-100,000 simulations per analysis) (Fig 4, Fig 4-Source Data 1). For our outcome measure, we used Tot.TMD since all TMD measures (i.e., Cent.TMD, Haem.TMD, and Neur.TMD) were found to be significantly different using t-tests in the previous section. First, we estimated the power of the global test in discriminating high Tot.TMD in *bmp1a*$^{-/-}$ fish as a function of sample size and alpha value (Fig 4A). We found that a power of >0.8 was attained with a sample size of n=3, 4, and 6 fish/group for alpha values of 0.05, 0.01, and 0.001, respectively. Next, using a sample size of n=3 fish/group and alpha=0.05, we estimated test sensitivity (fraction of times in which p<0.05 when comparing *bmp1a*$^{-/-}$ fish to WT fish) (Fig 4B) and specificity (1 - fraction of times in which p<0.05 when comparing WT to WT fish) (Fig 4C) for a) the global test (using vertebrae 1:20, scanned at 21µm resolution), b) t-tests of averaged quantities (using the mean of vertebrae 1:20, scanned at 21µm

bioRxiv preprint doi: https://doi.org/10.1101/105569; this version posted March 2, 2017. The copyright holder for this preprint (which was not certified by peer review) is the author/funder. All rights reserved. No reuse allowed without permission.

resolution), and c) t-tests of individual vertebrae (using vertebra 2, scanned at 10.5µm resolution). We found that the global test conferred higher sensitivity, with similar specificity, compared to t-tests of averaged quantities as well as t-tests of individual vertebrae, even when the latter was performed at higher resolution. For instance, at alpha=0.05, the sensitivity of the global test, t-test of individual vertebrae, and t-test of averaged quantities was 0.92, 0.87, and 0.82. At alpha=0.01, the sensitivity of the global test, t-test of individual vertebrae, and t-test of averaged quantities was 0.56, 0.42, and 0.37 (respectively). Specificity values were consistent with those predicted from specified levels of alpha: as an example, at alpha=0.01, specificity was 0.99 in all three cases. For alpha=0.05 and n=3, we estimated a false discovery rate of 4.4% for the global test procedure. Finally, we compared the power of the different testing procedures as a function of effect size (Fig 4D,E). We found that the global test conferred higher power compared to t-tests of averaged quantities and t-tests of individual vertebrae, with the relative increase greatest at small effect sizes (e.g., ~1.3 to 1.4 fold greater at an effect size of 0.5, compared to ~1.1 to 1.2 fold greater at an effect size of 3).

To corroborate our simulations experimentally, we used the n=3 WT and *bmp1a*$^{-/-}$ fish described in the previous section to form 15 different groupings with n=2 fish/group (Fig 4-Figure Supplement 1): 9 groupings compared fish of different genotypes (i.e., WT vs. mutant), and 6 groupings compared fish of the same genotype (WT vs. WT or mutant vs. mutant). When we computed p-values using the different groupings (Fig 4F), we found that global tests conferred lower p-values when comparing WT vs. mutant (suggesting higher sensitivity), with similar p-values when comparing fish of the same genotype (suggesting similar sensitivity), compared to both t-tests of averaged quantities as well as t-tests of individual of vertebrae scanned at high resolution. Notably, for 4/9 (44%) of the WT vs. mutant comparisons we found a significant difference (i.e., $p<0.05$) between groups, comparable to the power of 0.58 we estimated for a sample size of n=2

bioRxiv preprint doi: https://doi.org/10.1101/105569; this version posted March 2, 2017. The copyright holder for this preprint (which was not certified by peer review) is the author/funder. All rights reserved. No reuse allowed without permission.

fish/group in Fig 4A. In contrast, only 1/9 (11%) of the WT vs. mutant comparisons were significantly different when performing t-tests of averaged quantities, and 0/9 (0%) when using individual vertebrae scanned at high resolution.

Identification of Novel Phenotypic Features in Known Axial Skeletal Mutants

We next performed comprehensive phenotypic characterization of *bmp1a*$^{-/-}$ fish, as well as another mutant associated with human brittle bone disease, *plod2*$^{-/-}$ [14]. Mutations in *PLOD2* are associated with Bruck syndrome, a recessive condition resembling OI. Previous studies revealed high vertebral BMD in adult zebrafish with mutants in *bmp1a*, [15], however, it is unclear whether this high BMD is attributable to an increase in bone mass, and/or mineralization. For *plod2*$^{-/-}$ mutants, adult animals were found to exhibit vertebral compressions, distorted vertebrae, and excessive bone formation [14]. Previous microCT analyses showed higher Centrum TMD in these mutants. However, due to the lack of robust methods to analyze the highly dysmorphic vertebrae in *plod2*$^{-/-}$ fish, previous microCT analyses were performed in two dimensional maximum intensity projections [14], and an in-depth, three dimensional phenotypic characterization of *plod2*$^{-/-}$ fish has yet to be performed.

Using FishCuT, we analyzed whole-body scans of *bmp1a*$^{-/-}$ and *plod2*$^{-/-}$ mutant fish, and compared them to WT sibling controls (n=3/group) (Fig 5, Fig 5-Source Data 1). Note that for the rest of our studies, to focus our analyses we restrict our presentation of results to ten traits (the nine possible combinations of (Cent, HA, NA) x (Vol, TMD, and Th), plus Cent.Le) and the 16 most anteriorly-located vertebrae. In *bmp1a*$^{-/-}$ mutants, analysis revealed significant increases in both bone mass and mineralization. Specifically, in regard to bone mass, centrum volume was significantly increased (Cent.Vol: p=0.007). Further, bone thickness was significantly elevated in all skeletal elements (Cent.Th: p=0.0007, Haem.Th: p=0.048, Neur.Th: p=0.005). No significant

bioRxiv preprint doi: https://doi.org/10.1101/105569; this version posted March 2, 2017. The copyright holder for this preprint (which was not certified by peer review) is the author/funder. All rights reserved. No reuse allowed without permission.

differences were observed with respect to haemal/neural arch volume (Haem.Vol: p=0.07, Neur.Vol: p=0.16) or centrum length (Cent.Le: p=0.051). In regard to bone mineralization, TMD was significantly elevated in all skeletal elements (Cent.TMD: p=0.003, Haem.TMD: p=0.006, Neur.TMD: p=0.006). While Cent.TMD and Neur.TMD appeared to be uniformly elevated across all vertebrae, Haem.TMD appeared to be differentially elevated in precaudal (first ten) vertebrae. We used the *covariates* functionality in the *globaltest* package in *R* to identify vertebral clusters that exhibit a significant association with genotype. We found that only vertebrae 2, 3, 4, and 7 were significantly associated with genotype (Fig 5-Figure Supplement 1), consistent with the notion that precaudal vertebrae were differentially affected.

For *plod2*$^{-/-}$ mutants (S.L. of WT: 27.9±0.7mm, S.L. of mutant: 20.2±1.1mm, mean±SD) (Fig 6, Fig 6-Source Data 1), we found that FishCuT robustly segmented vertebrae, despite severe vertebral malformations. Consistent with previous studies, we observed significantly elevated TMD in the centrum (Cent.TMD: p=0.038) but not haemal/neural arches (Haem.TMD: p=0.91, Neur.TMD: p=0.53) [14]. Further, we observed a significant decrease in centrum length (Cent.Le: $p=6.5\times10^{-5}$), as reported previously [14]. Morphologically, *plod2*$^{-/-}$ mutants exhibited a low bone mass phenotype in the haemal and neural arches (Haem.Vol: p=0.018, Neur.Vol: p=0.012), but not centrum (p=0.15). Further, *plod2*$^{-/-}$ mutants exhibited decreased haemal and neural arch thickness (Haem.Th: p=0.13, Neur.Th: p=0.034), but not centrum thickness (p=0.47).

Allometric Models Aid in Discriminating Mutant Phenotypes Masked by Alterations in Growth

In zebrafish, developmental progress is more closely related to standard length than to age [24, 25]. In analyzing mutants that exhibit differences in body size (e.g., *plod2*$^{-/-}$ mutants exhibited severely diminished body size compared to WT siblings), it is

bioRxiv preprint doi: https://doi.org/10.1101/105569; this version posted March 2, 2017. The copyright holder for this preprint (which was not certified by peer review) is the author/funder. All rights reserved. No reuse allowed without permission.

difficult to discriminate to what degree altered phenotypes are attributable to differences in developmental progress, versus specific effects on skeletal function. Furthermore, although morphological developmental milestones can sometimes allow staging despite genotype-specific differences in size and growth during the larval-to-adult transformation, few such milestones have been identified, particularly during later stages, and some milestones are themselves skeletal traits, necessitating an alternative approach. To help address these challenges, we developed allometric models to control for effects of body size during phenomic analysis. We performed an ontogenetic series by phenomically profiling WT fish over a range of standard lengths (18.4mm to 31.8mm, n=12) (Fig 7-Figure Supplement 1). To model each trait in WT fish as a function of standard length, we used a standard power-law relationship for allometric modeling [26]: $y=ax^b$, where y is the trait of interest, x is standard length, and a and b are empirically-derived parameters. The scaling exponent b is directly interpretable when quantities are associated with mass, length, area, and volume. Thus, we converted TMD to a mass-based quantity by computing tissue mineral content (TMC, mgHA) as the product of volume and TMD in each skeletal element (e.g., Cent.TMC = Cent.Vol*Cent.TMD). In general, we found that most traits significantly deviated from isometric growth (i.e., proportional relationships were not preserved with growth) with respect to standard length (Table 1). Specifically, traits associated with thickness and volume exhibited negative allometry (scaling exponents lower than those expected for isometric growth), while TMC exhibited positive allometry. We used the following relationship to normalize for allometric effects of growth [26]: $y^* = y\ (x^*/x)^b$, where y is the trait of interest, x is standard length, x* is a reference standard length, and y* is the transformed value. When we applied this relationship to the phenomic profiles from the WT animals in our ontogenetic series (using the mean standard length of all WT fish as the reference standard length), we found that the coefficient of variability was substantially reduced

bioRxiv preprint doi: https://doi.org/10.1101/105569; this version posted March 2, 2017. The copyright holder for this preprint (which was not certified by peer review) is the author/funder. All rights reserved. No reuse allowed without permission.

compared to unnormalized values, as well as when quantities were normalized by an alternate transformation, 1/S.L. (Fig 7, Fig 7-Source Data 1).

Next, we used the above normalization procedure to re-analyze *plod2*$^{-/-}$ mutants. We scaled phenotypic data in WT sibling controls by applying Eq. 2, using the mean standard length of *plod2*$^{-/-}$ mutants as the reference length. In our unnormalized analysis of *plod2*$^{-/-}$ fish (i.e., Fig 6), we observed significant decreases in several morphological quantities including Haem.Vol, Haem.Th, Neur.Vol, Neur.Th, and Cent.Le. In contrast to these low bone mass phenotypes we did not observe any differences in these traits following normalization (Haem.Vol: p=0.23, Haem.Th: p=0.33, Neur.Vol: p=0.58, Neur.Th: p=0.56, Cent.Le: p=0.39) (Fig 8, Fig 8-Source Data 1). Instead, we observed a significant *increase* in Cent.Vol (p=0.003). Further, we observed a significant increase in centrum, haemal arch, and neural arch TMD (Cent.TMD: p=0.0001, Haem.TMD: p=0.002, Neur.TMD: p=0.002). Since Cent.Le (p=0.39) and Cent.Th (p=0.08) were similar in *plod2*$^{-/-}$ fish and WT siblings, we surmised that the increase in Cent.Vol may be attributable to an increase in centrum diameter. Consistent with this notion, when we manually examined transverse sections in microCT images (Fig 8L), we observed a clear increase in centrum diameter in *plod2*$^{-/-}$ mutants relative to similarly-sized, non-sibling WT animals (and to a lesser extent, larger, sibling controls). This phenotype was not previously identified during the initial characterization of the *plod2*$^{-/-}$ mutant line [27], and is reminiscent of the cortical expansion that occurs in mammals due to coupled bone formation and resorption on the periosteal and endosteal surface, respectively. Collectively, these analyses identify a novel phenotypic feature, centrum expansion, in *plod2*$^{-/-}$ mutants, and suggest the utility of phenomic-based allometric models as a complimentary analytical tool to reveal mutant phenotypes masked by variations in growth.

bioRxiv preprint doi: https://doi.org/10.1101/105569; this version posted March 2, 2017. The copyright holder for this preprint (which was not certified by peer review) is the author/funder. All rights reserved. No reuse allowed without permission.

Identification of opallus *as a Novel Axial Skeletal Mutant*

Finally, based on the potential for FishCuT to identify novel phenotypes in known skeletal mutants, we examined the potential for FishCuT to identify novel axial skeletal mutants among fish populations derived from forward genetic screens. *opallus* was derived from a forward genetic screen, and exhibits pigmentation abnormalities characterized by excessive xanthophores and depleted melanophores, as well as jaw hypertrophy [28]. *opallus* harbors a mutation in thyroid stimulating hormone receptor (*tshr*) identical to a human mutation causing constitutive TSHR activity and hyperthyroidism [28]. These two conditions have been associated with opposing effects on human BMD. Specifically, while hyperthyroidism is traditionally associated with low BMD, TSHR gain-of-function has been associated with high BMD [29]; it was unknown whether *opallus* exhibited an axial skeletal phenotype. In a first cohort where we performed an initial screen of n=2 fish (Fig 9A), we observed a clear increase in TMD in *opallus* that was not present in standard length-matched AB controls, or in another mutant derived in a forward genetic screen that exhibits pigmentation defects, *pissarro* [30] (S.L. of AB: 23.7±1.1mm, S.L. of *opallus*: 24.3±1.4mm, S.L. of *pissarro*: 23.7±0.1mm, mean±SD). Follow up analyses (n=5/group, S.L. of AB: 23.7±0.5mm, S.L. of *opallus*: 24.3±1.4mm, mean±SD) revealed that *opallus* exhibited a significant increase in centrum, haemal arch, and neural arch TMD (Cent.TMD: p=0.012, Haem.TMD: p=0.009, Neur.TMD: p=0.006) (Fig 9B-K, Fig 9-Source Data 1). Morphologically, most traits were normal (Cent.Vol: p=0.88, Haem.Vol: p=0.20, Cent.Th: p=0.12, Haem.Th: p=0.38, Neur.Th: p=0.38, Cent.Le: p=0.29) except for neural arch volume, which was significantly decreased in *opallus* (Neur.Vol: p=0.002). This decrease was most pronounced in anterior vertebrae, with covariate analysis revealing significant associations between vertebrae 1-5 and genotype (Fig 9-Figure Supplement 1).

bioRxiv preprint doi: https://doi.org/10.1101/105569; this version posted March 2, 2017. The copyright holder for this preprint (which was not certified by peer review) is the author/funder. All rights reserved. No reuse allowed without permission.

DISCUSSION

In this study, we developed microCT-based methods and a segmentation algorithm, FishCuT, enabling rapid (<5min/fish), whole-body profiling of hundreds of morphological and densitometric traits in the axial skeleton of adult zebrafish. We profiled over 20,000 data points derived from over ~2500 skeletal elements in wildtype fish of different degrees of developmental progress as well as mutant lines associated with human disease. By performing large-scale phenomic analysis in a single organ system, our studies reveal virtues of deep phenotyping at the whole-organism scale.

A challenge to the analysis of high-dimensional phenotypic data is the curse of dimensionality: when testing for changes in each trait individually, as a consequence of multiple testing correction, the number of samples required for a statistically reliable result increases exponentially as the number of traits is increased. In lieu of analyzing each trait in isolation, we examined whether patterns of element/outcome combinations varied across vertebral bodies were altered in mutant populations. In Monte Carlo simulations, when holding alpha constant, power in the global test was consistently higher compared to t-tests of averaged quantities and t-tests of individual vertebrae, with the relative increase in power greatest at small effect sizes. Further, simulated levels of specificity were consistent with specified values of alpha. Our studies suggest that vertebral phenomic patterns may confer enhanced sensitivity in discriminating mutant phenotypes relative to analyzing individual vertebrae, even when the latter is performed at higher resolution. This attribute may increase productivity in forward genetic screens, as well as provide opportunities to study genetic variants of smaller effect size, such as those which underlie the overwhelming majority of complex diseases [31]. Our studies also challenge the concept that higher sensitivity in discriminating mutant populations must come at the cost of higher microCT scan resolution and hence, lower throughput, since microCT scanning of the whole body at medium resolution can be performed in a

bioRxiv preprint doi: https://doi.org/10.1101/105569; this version posted March 2, 2017. The copyright holder for this preprint (which was not certified by peer review) is the author/funder. All rights reserved. No reuse allowed without permission.

similar amount of time as a few vertebrae at high-resolution. While our workflow is highly sensitive in discriminating mutants that exhibit subtle phenotypic alterations in a large number of bones, other scan resolutions and statistical testing may be appropriate in some cases. For instance, while we found that scans acquired at 21µm and 10.5µm resolution were comparable in their analysis of *bmp1a*$^{-/-}$ mutants, it is possible that other mutant lines may present extremely small, thin, or hypomineralized structures that require greater scanning resolution to resolve. Finally, given the fact that the global test exhibits optimal power when many features exhibit minor changes [18], our workflow will be most optimal when there are many small changes in a large number of vertebrae, and other statistical tests may be more powerful when testing for larger effects in a single (or few) vertebrae.

By performing in-depth, whole-body phenotyping in *bmp1a*$^{-/-}$ and *plod2*$^{-/-}$ mutants, our studies shed new light on multivariate phenotypes in the zebrafish skeleton associated with human skeletal disease. While *bmp1a*$^{-/-}$ and *plod2*$^{-/-}$ mutants exhibited differing effects on indices of bone mass and microarchitecture, both mutants exhibited high TMD. This phenotype is consistent with the bone over-mineralization that is a hallmark of brittle bone disease [32]. While *bmp1a*$^{-/-}$ mutants exhibit increased TMD in all vertebral compartments (centrum, haemal arch, and neural arch), *plod2*$^{-/-}$ fish exhibit high TMD in the centrum only. Further, the elevation in haem.TMD in *bmp1a*$^{-/-}$ mutants was focused primarily to anteriorly-located vertebrae. Phenotypic abnormalities in human OI has been shown to vary among patients and anatomical site [33]. The segregation of phenotypic abnormalities to different anatomical sites is likely to provide important clues into disease pathology; our workflow provides a unifying framework to systematically analyze the mechanistic basis of site-specific segregation of phenotypic abnormalities.

bioRxiv preprint doi: https://doi.org/10.1101/105569; this version posted March 2, 2017. The copyright holder for this preprint (which was not certified by peer review) is the author/funder. All rights reserved. No reuse allowed without permission.

Since developmental progress in zebrafish is more closely related to standard length than to age, the interpretation of mutant phenotypes can substantially differ depending on whether mutants are compared to age-matched WT siblings (which may differ in standard length and thus developmental progress), or non-sibling WT animals matched by standard length (which could mask genetic alterations on developmental progress, and exhibit greater variation in genetics and environmental influences). In high-throughput settings where resource conservation is critical, it is not practical to dedicate resources for both experimental comparisons. Our studies demonstrate that allometric modeling is effective in transforming WT sibling data to a "virtual" phenome scaled to the mean standard length of age-matched mutants, providing a computational means to enable both length- and age-matched fish comparisons from a single control group. Using this approach, we identified expanded centrum diameter in *plod2*$^{-/-}$ mutants. In mammals, cortical expansion arises due to bone remodeling, with bone formation on the periosteal surface coupled with resorption on the endosteal surface. Thus, our studies bring forth the question of whether the increased centrum diameter in *plod2*$^{-/-}$ mutants is attributable to accelerated bone remodeling.

In addition to identifying novel phenotypes in known skeletal mutants, we also identified a novel axial skeletal mutant, *opallus*, harboring a TSHR gain-of-function mutation. Excess TSHR activity has been associated with high BMD in humans [29]. Notably, unlike *plod2*$^{-/-}$ and *bmp1a*$^{-/-}$ mutants, *opallus* exhibited high TMD in the presence of mostly normal bone mass and morphology, providing evidence of the potential for these traits to be decoupled in zebrafish mutants. By virtue of the wealth of genetic resources in zebrafish (as of January 2017, >17,000 mutant alleles are available to order through the Zebrafish Mutation Project [34]), the ability to quickly generate new mutant alleles using CRISPR/Cas9, and the ability for individual labs to house thousands of adult animals, our studies establish successful practices to merge high-content

bioRxiv preprint doi: https://doi.org/10.1101/105569; this version posted March 2, 2017. The copyright holder for this preprint (which was not certified by peer review) is the author/funder. All rights reserved. No reuse allowed without permission.

phenotyping with genetic analysis to identify new genes mediating human skeletal health. In this context, the construction of large collections of phenomes in zebrafish mutants whose orthologs are associated with mammalian bone mass and mineral accrual is likely to facilitate not only the identification of novel regulators of human bone mass, but also phenotypic signatures in zebrafish that are predictive of human skeletal disease.

A future challenge is to increase the throughput and content of our workflow. Since FishCuT supports the DICOM standard, it is readily ported to other microCT systems. In this context, commercial microCT systems optimized for rapid throughput imaging (e.g., through the use larger detectors to increase the number of animals per field of view, higher power x-ray sources to decrease sampling time per image, and robot-based sample changing systems) have been shown to increase imaging throughput by 10 fold or more [35]. Further, Mader et al. described a high-throughput, fully automatic system for synchrotron-based tomographic microscopy that enabled analysis of 1300 mouse femurs [7]. In regard to image analysis, machine learning-based approaches enable fully automated localization of boundaries of vertebral bodies in human CT/MR data [36], and such an approach might be used to automate seeding of segment boundaries, particularly if analysis is restricted to mutants that do not exhibit severe dysmorphic phenotypes. Finally, a long-term challenge is to extend analysis to other skeletal structures, including the craniofacial skeleton. Notably, as microCT scans are archived, these image libraries can be retroactively analyzed as new algorithms are developed, and re-analyzed to identify new genotype-to-phenotype associations.

In conclusion, we have developed a sensitive, rapid workflow for microCT-based skeletal phenomics in adult zebrafish. Our studies provide a foundation to systematically

bioRxiv preprint doi: https://doi.org/10.1101/105569; this version posted March 2, 2017. The copyright holder for this preprint (which was not certified by peer review) is the author/funder. All rights reserved. No reuse allowed without permission.

map genotype-to-phenome relationships as a path toward rapid advances in our understanding of the genetic basis of adult skeletal health.

MATERIALS AND METHODS

Zebrafish Rearing

All studies were performed on an approved protocol in accordance with the University of Washington Institutional Animal Care and Use Committee (IACUC). Zebrafish were housed at a temperature of 27°C–29°C on a 14:10 h light:dark photoperiod. Studies were conducted in mixed sex adult zebrafish. WT ARO and AB fish were obtained from Aquatic Research Organisms [37] and the Zebrafish International Resource Center (ZIRC, http://zebrafish.org), respectively. *opallus*^{b1071} [28] and *pissarro*^{utr8e1} [30] were isolated in forward genetic screens. *bmp1a*^{sa2416} and *plod2*^{sa1768} mutant zebrafish were generated by the Zebrafish Mutation Project (ZMP) and obtained from ZIRC [34]. For all mutant lines, heterozygous mutant zebrafish were incrossed to obtain homozygous mutants. All fish were housed in plastic tanks on a commercial recirculating aquaculture system. At the desired time point, zebrafish were euthanized by MS-222 overdose or immersion in ice water. For storage, fish were either frozen at -20°C, or fixed in 4% PFA. Comparisons were only performed in fish subjected to the same storage procedure.

MicroCT Scanning

MicroCT scanning was performed using a vivaCT40 (Scanco Medical, Switzerland). Medium-resolution scans (21µm voxel resolution) were acquired using the following settings: 55kVp, 145µA, 1024 samples, 500proj/180°, 200ms integration time. High-resolution scans (10.5µm voxel resolution) were acquired using the following settings: 55kVp, 145µA, 2048 samples, 1000proj/180°, 200ms integration time. DICOM files of individual fish were generated using Scanco software, and analyzed using the

bioRxiv preprint doi: https://doi.org/10.1101/105569; this version posted March 2, 2017. The copyright holder for this preprint (which was not certified by peer review) is the author/funder. All rights reserved. No reuse allowed without permission.

custom software described below. In general, at least two fish were scanned simultaneously in each acquisition.

Image Analysis

Image processing methods were implemented as custom software developed in MATLAB (scripts were tested in v2016.a). To encourage open-source development, we implemented the MIJI package to enable calls to libraries and functions developed in FIJI/ImageJ [38, 39]. Further, we developed a graphical user interface (GUI) to facilitate user interaction. Analysis consists of several stages. Stage 1 consists of preprocessing, for which we have implemented a preprocessing module in which the user is able to specify a rotation along the anteroposterior axis to orient specimens to an upright position. This module also enables slice-by-slice visualization, as well as mean or maximum intensity projections of unprocessed DICOM images.

Stage 2 consists of thresholding. In general, we have found that fish within and across clutches can exhibit significant differences in mineralization, and thus cannot be reliably analyzed using a uniform threshold value. Thus, we calculate thresholds for each animal using a semi-automatic approach. To filter out background, the user draws a ROI outlining the fish in a maximum intensity projection, all values outside this region of interest are set to 0, and the threshold is calculated using the IsoData algorithm in ImageJ [19, 20]. The threshold value may be adjusted by multiplying it by a correction factor to provide more conservative or stringent thresholding, depending on user needs. Based on a comparison of user defined thresholds and those computed using the approach described above, we multiplied the IsoData threshold by 0.73 across all experiments.

bioRxiv preprint doi: https://doi.org/10.1101/105569; this version posted March 2, 2017. The copyright holder for this preprint (which was not certified by peer review) is the author/funder. All rights reserved. No reuse allowed without permission.

Stage 3 consists of vertebral segmentation. Our approach is to isolate individual vertebrae so that each vertebra is composed of one or more connected components that do not contain voxels from different vertebra. The user initiates planes of separation between vertebra by drawing a "separation line" between each pair of centra. Voxels within a plane defined by the separation line are set to 0, the connected components are computed, and connected component labels are tallied for each of the two volumes separated by the plane. If the connected components with the plurality of votes in the two regions are distinct, the algorithm stops; otherwise, the separation line is extended, and the process repeated. While we found this approach robustly separated centra in all samples (including those that exhibited significant morphological deficits, see below), we encountered some cases in which ribs close to pterygiophores and associated fin rays would be considered as a single connected structure. In this case, we have implemented a manual "cutting" tool to provide the user with the ability to sever connections between skeletal elements.

Stage 4 consists of vertebral assignment. Here, the user identifies each vertebrae's components using a user-interactive, color-coded map of connected components.

Stage 5 consists of neural arch, centrum, and haemal arch segmentation. Using a supervised algorithm, FishCuT creates 3D image masks of the three regions for each vertebral body. The 3D masks are formed in part by utilizing the user's inputs to the separation-plane growing algorithm, i.e. the endpoints of the line separating adjacent centra. We create the 3D neural arch mask as the entire region above the line extended between the two upper-most inputs for a vertebra. The centrum mask is defined by the region inside all 4 points for a vertebra. We include an adjustable buffer, with a default of five voxels, surrounding the centrum mask. The haemal arch mask is defined by

bioRxiv preprint doi: https://doi.org/10.1101/105569; this version posted March 2, 2017. The copyright holder for this preprint (which was not certified by peer review) is the author/funder. All rights reserved. No reuse allowed without permission.

substracting the region of the vertebrae from the regions defined by the centrum and neural arch masks. All segmentations can be visually inspected from an outputted image file containing colored-coded regions superimposed on the original image.

Stage 6 is the calculation of phenotypic traits. Local thickness is computed using a model-independent method [40] implemented as the Local Thickness plugin in ImageJ [41]. Volume and surface area were computed using the *nnz* and *bwperim* functions in MATLAB. TMD was computed using the following relationship: $mgHA/cm^3$ = (x/4096)*slope+intercept, where x = the pixel intensity in the DICOM image, and the values for slope (281.706) and intercept (-195.402) were acquired during scanner calibration.

Statistical Analysis

For mutant fish with a known axial skeletal phenotype (*bmp1a*$^{-/-}$ and *plod2*$^{-/-}$), results are reported from a single experiment; for mutant fish with a newly identified axial skeletal phenotype, results are reported from two experiments (an initial screen with n=2 fish/group, followed by follow up analysis with n=5 fish/group). Each biological replicate represents one technical replicate. Outliers were not identified in the study. All statistical analyses were performed in GraphPad Prism or R [42]. For comparisons of medium and high scanning resolution, linear regressions were performed with intercept set to zero. Two tailed t-tests with unequal variances were used for univariate analysis between two groups. In all other cases, multivariate analysis was performed using the globaltest package [18, 19]. $p<0.05$ was considered statistically significant in all cases.

ACKNOWLEDGEMENTS

Research reported in this publication was supported by the National Institute of Arthritis and Musculoskeletal and Skin Diseases (NIAMS) of the National Institutes of

bioRxiv preprint doi: https://doi.org/10.1101/105569; this version posted March 2, 2017. The copyright holder for this preprint (which was not certified by peer review) is the author/funder. All rights reserved. No reuse allowed without permission.

Health (NIH) under Award Number AR066061. The content is solely the responsibility of the authors and does not necessarily represent the official views of the National Institutes of Health. RYK also acknowledges support from UW Royalty Research Fund Grant A88052, the University of Washington Department of Orthopedics and Sports Medicine. SKM acknowledges support from NIH K99/R00 GM105874. DMP acknowledges support from NIH R01 GM11233. PC acknowledges support from the Belgian Science Policy Office Interuniversity Attraction Poles (BELSPO-IAP) program through the project IAP P7/43-BeMGI. ZIRC is supported by NIH grant RR12546.

bioRxiv preprint doi: https://doi.org/10.1101/105569; this version posted March 2, 2017. The copyright holder for this preprint (which was not certified by peer review) is the author/funder. All rights reserved. No reuse allowed without permission.

REFERENCES

1. Houle, D., D.R. Govindaraju, and S. Omholt, *Phenomics: the next challenge.* Nat Rev Genet, 2010. **11**(12): p. 855-66.

2. Schork, N.J., *Genetics of complex disease: approaches, problems, and solutions.* Am J Respir Crit Care Med, 1997. **156**(4 Pt 2): p. S103-9.

3. Bilder, R.M., et al., *Phenomics: the systematic study of phenotypes on a genome-wide scale.* Neuroscience, 2009. **164**(1): p. 30-42.

4. Adams, D., et al., *Identification of New Models for Bone Research via High-Throughput Screening of Mice from the Knockout Mouse Project.* Transactions of the Orthopaedics Research Society, 2015.

5. Dyment, N.A., et al., *High-Throughput, Multi-Image Cryohistology of Mineralized Tissues.* J Vis Exp, 2016(115).

6. Hong, S.H., et al., *Computer-Automated Static, Dynamic and Cellular Bone Histomorphometry.* J Tissue Sci Eng, 2012. **Suppl 1**: p. 004.

7. Mader, K.S., et al., *High-throughput phenotyping and genetic linkage of cortical bone microstructure in the mouse.* Bmc Genomics, 2015. **16**.

8. Pardo-Martin, C., et al., *High-throughput hyperdimensional vertebrate phenotyping.* Nature Communications, 2013. **4**.

9. Buchan, J.G., et al., *Kinesin Family Member 6 (kif6) Is Necessary for Spine Development in Zebrafish.* Developmental Dynamics, 2014. **243**(12): p. 1646-1657.

10. Gray, R.S., et al., *Loss of col8a1a function during zebrafish embryogenesis results in congenital vertebral malformations.* Developmental Biology, 2014. **386**(1): p. 72-85.

bioRxiv preprint doi: https://doi.org/10.1101/105569; this version posted March 2, 2017. The copyright holder for this preprint (which was not certified by peer review) is the author/funder. All rights reserved. No reuse allowed without permission.

11. Bouxsein, M.L., et al., *Guidelines for assessment of bone microstructure in rodents using micro-computed tomography.* J Bone Miner Res, 2010. **25**(7): p. 1468-86.

12. Cheng, K.C., et al., *Whole-animal imaging, gene function, and the Zebrafish Phenome Project.* Current Opinion in Genetics & Development, 2011. **21**(5): p. 620-629.

13. Fisher, S., P. Jagadeeswaran, and M.E. Halpern, *Radiographic analysis of zebrafish skeletal defects.* Dev Biol, 2003. **264**(1): p. 64-76.

14. Gistelinck, C., et al., *Loss of Type I Collagen Telopeptide Lysyl Hydroxylation Causes Musculoskeletal Abnormalities in a Zebrafish Model of Bruck Syndrome.* J Bone Miner Res, 2016. **31**(11): p. 1930-1942.

15. Asharani, P.V., et al., *Attenuated BMP1 function compromises osteogenesis, leading to bone fragility in humans and zebrafish.* Am J Hum Genet, 2012. **90**(4): p. 661-74.

16. Spoorendonk, K.M., et al., *Retinoic acid and Cyp26b1 are critical regulators of osteogenesis in the axial skeleton.* Development, 2008. **135**(22): p. 3765-74.

17. Burghardt, A.J., et al., *Quantitative assessment of bone tissue mineralization with polychromatic micro-computed tomography.* Calcif Tissue Int, 2008. **83**(2): p. 129-38.

18. Goeman, J.J., S.A. van de Geer, and H.C. van Houwelingen, *Testing against a high dimensional alternative.* Journal of the Royal Statistical Society Series B-Statistical Methodology, 2006. **68**: p. 477-493.

19. Goeman, J.J., et al., *A global test for groups of genes: testing association with a clinical outcome.* Bioinformatics, 2004. **20**(1): p. 93-99.

20. Zou, K.H., et al., *Statistical validation of image segmentation quality based on a spatial overlap index.* Acad Radiol, 2004. **11**(2): p. 178-89.

bioRxiv preprint doi: https://doi.org/10.1101/105569; this version posted March 2, 2017. The copyright holder for this preprint (which was not certified by peer review) is the author/funder. All rights reserved. No reuse allowed without permission.

21. Zijdenbos, A.P., et al., *Morphometric analysis of white matter lesions in MR images: method and validation.* IEEE Trans Med Imaging, 1994. **13**(4): p. 716-24.

22. Asharani, P.V., et al., *Attenuated BMP1 Function Compromises Osteogenesis, Leading to Bone Fragility in Humans and Zebrafish.* American Journal of Human Genetics, 2012. **90**(4): p. 661-674.

23. Rittweger, J., et al., *Adjusting for the partial volume effect in cortical bone analyses of pQCT images.* J Musculoskelet Neuronal Interact, 2004. **4**(4): p. 436-41.

24. Parichy, D.M., et al., *Normal table of postembryonic zebrafish development: staging by externally visible anatomy of the living fish.* Dev Dyn, 2009. **238**(12): p. 2975-3015.

25. McMenamin, S.K., M.N. Chandless, and D.M. Parichy, *Working with zebrafish at postembryonic stages.* Zebrafish: Cellular and Developmental Biology, Pt B: Developmental Biology, 2016. **134**: p. 587-607.

26. Lleonart, J., J. Salat, and G.J. Torres, *Removing allometric effects of body size in morphological analysis.* J Theor Biol, 2000. **205**(1): p. 85-93.

27. Gistelinck, C., et al., *Loss of Type I Collagen Telopeptide Lysyl Hydroxylation Causes Musculoskeletal Abnormalities in a Zebrafish Model of Bruck Syndrome.* J Bone Miner Res, 2016.

28. McMenamin, S.K., et al., *Thyroid hormone-dependent adult pigment cell lineage and pattern in zebrafish.* Science, 2014. **345**(6202): p. 1358-61.

29. de Lloyd, A., et al., *TSH receptor activation and body composition.* J Endocrinol, 2010. **204**(1): p. 13-20.

30. Quigley, I.K., et al., *Pigment pattern evolution by differential deployment of neural crest and post-embryonic melanophore lineages in Danio fishes.* Development, 2004. **131**(24): p. 6053-69.

bioRxiv preprint doi: https://doi.org/10.1101/105569; this version posted March 2, 2017. The copyright holder for this preprint (which was not certified by peer review) is the author/funder. All rights reserved. No reuse allowed without permission.

31. Gibson, G., *Rare and common variants: twenty arguments.* Nat Rev Genet, 2012. **13**(2): p. 135-45.

32. Bishop, N., *Bone Material Properties in Osteogenesis Imperfecta.* J Bone Miner Res, 2016. **31**(4): p. 699-708.

33. Cassella, J.P., T.C. Stamp, and S.Y. Ali, *A morphological and ultrastructural study of bone in osteogenesis imperfecta.* Calcif Tissue Int, 1996. **58**(3): p. 155-65.

34. Kettleborough, R.N., et al., *A systematic genome-wide analysis of zebrafish protein-coding gene function.* Nature, 2013. **496**(7446): p. 494-7.

35. Wyatt, S.K., et al., *Fully-automated, high-throughput micro-computed tomography analysis of body composition enables therapeutic efficacy monitoring in preclinical models.* Int J Obes (Lond), 2015. **39**(11): p. 1630-7.

36. Chu, C., et al., *Fully Automatic Localization and Segmentation of 3D Vertebral Bodies from CT/MR Images via a Learning-Based Method.* PLoS One, 2015. **10**(11): p. e0143327.

37. Recidoro, A.M., et al., *Botulinum toxin induces muscle paralysis and inhibits bone regeneration in zebrafish.* J Bone Miner Res, 2014. **29**(11): p. 2346-56.

38. Schneider, C.A., W.S. Rasband, and K.W. Eliceiri, *NIH Image to ImageJ: 25 years of image analysis.* Nat Methods, 2012. **9**(7): p. 671-5.

39. Schindelin, J., et al., *Fiji: an open-source platform for biological-image analysis.* Nat Methods, 2012. **9**(7): p. 676-82.

40. Hildebrand, T. and P. Ruegsegger, *A new method for the model-independent assessment of thickness in three-dimensional images.* Journal of Microscopy-Oxford, 1997. **185**: p. 67-75.

41. Dougherty, R. and K.-H. Kunzelmann, *Computing Local Thickness of 3D Structures with ImageJ.* Microsc Microanal, 2007. **13**(S2): p. 1678 CD to 1679 CD.

bioRxiv preprint doi: https://doi.org/10.1101/105569; this version posted March 2, 2017. The copyright holder for this preprint (which was not certified by peer review) is the author/funder. All rights reserved. No reuse allowed without permission.

42. Team, R.C., *A language and environment for statistical computing*. 2015, Vienna, Austria: R Foundation for Statistical Computing.

bioRxiv preprint doi: https://doi.org/10.1101/105569; this version posted March 2, 2017. The copyright holder for this preprint (which was not certified by peer review) is the author/funder. All rights reserved. No reuse allowed without permission.

FIGURE LEGENDS

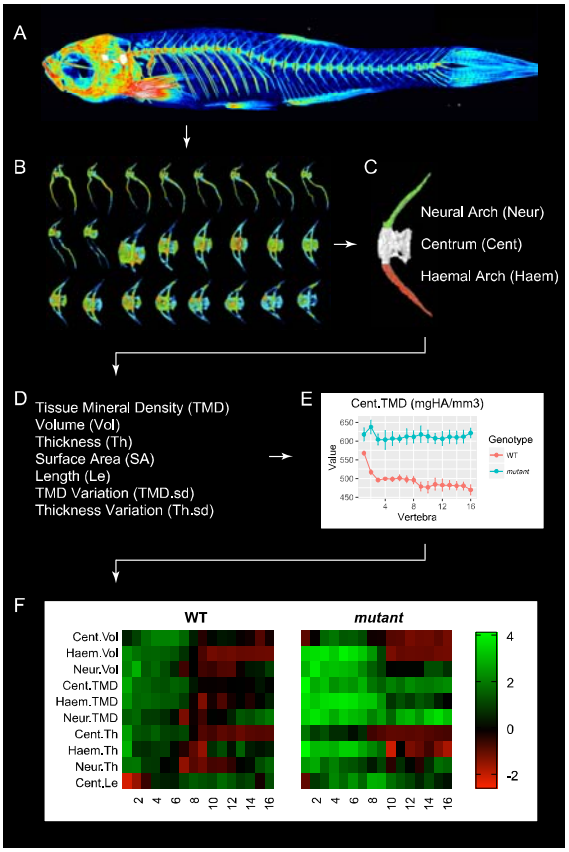

Figure 1. microCT-based phenomic profiling of the axial skeleton in adult zebrafish. (A) Whole-body microCT scans are acquired in adult fish (image shows maximum intensity projection of microCT scan volume, pseudo-colored to highlight skeletal structures). (B) Individual vertebrae are isolated using FishCuT (image shows 24 vertebrae from the same fish, colors indicate local thickness), and (C) each vertebral body is segmented into three skeletal elements: the Neural Arch (green), Centrum (white), and Haemal Arch/Pleural Ribs (red). (D) For each skeletal element, FishCuT computes the following parameters: Tissue Mineral Density, Volume, Thickness, Surface Area, Length (centrum only), Tissue Mineral Density Variation, and Thickness Variation. (E) For analysis, each combination of element/outcome is computed as a function of vertebra number, and subjected to the global test. Shown is a plot of one combination of element/outcomes, Cent.TMD, as a function of vertebra number in WT vs. mutant fish.

bioRxiv preprint doi: https://doi.org/10.1101/105569; this version posted March 2, 2017. The copyright holder for this preprint (which was not certified by peer review) is the author/funder. All rights reserved. No reuse allowed without permission.

(F) Standard scores are computed and arranged into "skeletal barcodes" that facilitate visualization of phenotypic trends both within individuals and across groups. Shown are the skeletal barcodes for a single WT (left) and mutant fish (right).

bioRxiv preprint doi: https://doi.org/10.1101/105569; this version posted March 2, 2017. The copyright holder for this preprint (which was not certified by peer review) is the author/funder. All rights reserved. No reuse allowed without permission.

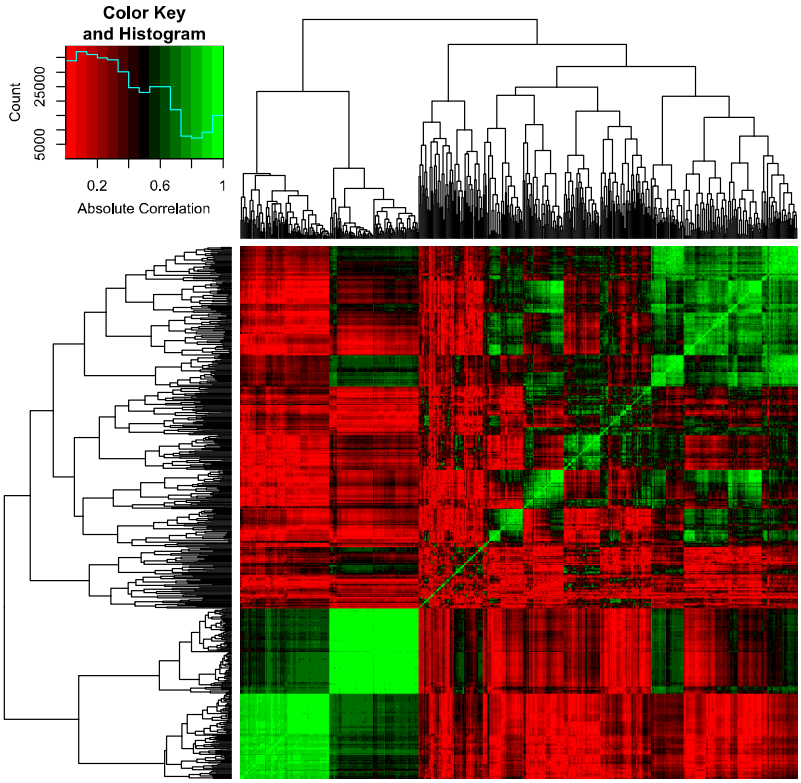

Figure 2. Phenotypic traits profiled by FishCuT exhibit low overall correlation. Results are shown for 600 different traits profiled in 34 different fish. Absolute Pearson correlation coefficients were computed between each pair of traits, resulting in a 600x600 correlation matrix. Results are plotted as a heatmap, and hierarchically clustered to facilitate visualization. The predominance of red regions suggests most trait pairs exhibit low correlation. The legend depicts a color scale as well as a histogram of absolute correlations; the median value of this distribution was 0.34.

bioRxiv preprint doi: https://doi.org/10.1101/105569; this version posted March 2, 2017. The copyright holder for this preprint (which was not certified by peer review) is the author/funder. All rights reserved. No reuse allowed without permission.

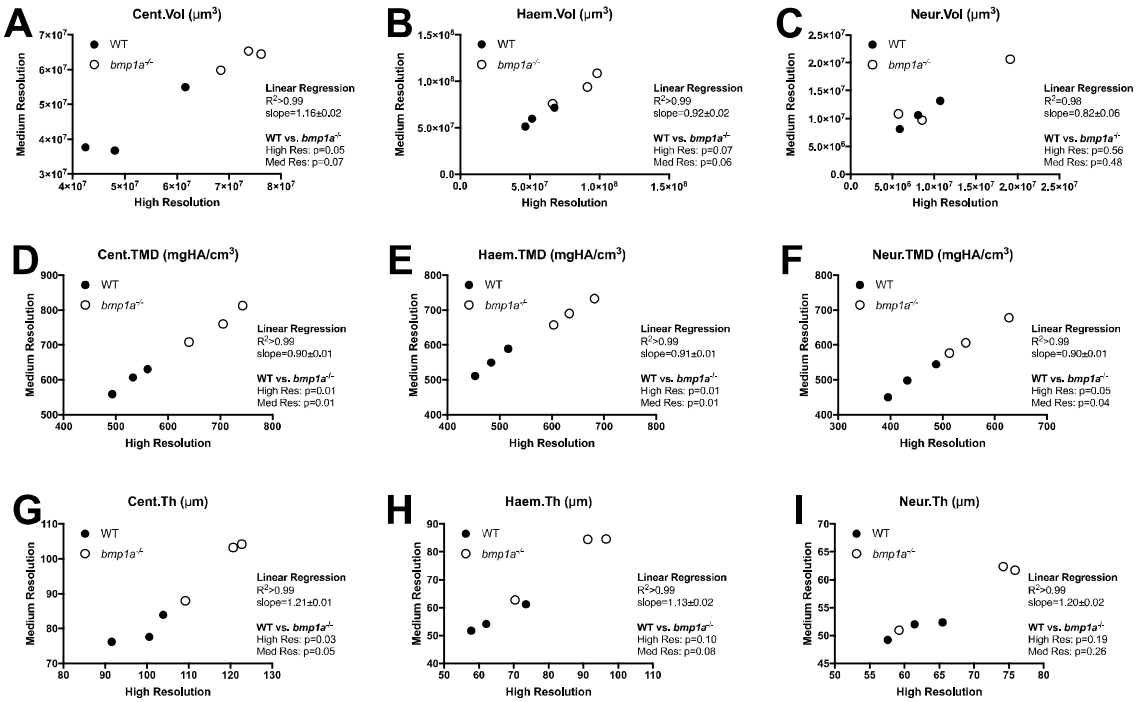

Figure 3. Analysis of WT and bmp1a-/- mutant fish reveals traits quantified via medium and high resolution microCT scans exhibit extremely high correlation. Results are shown for the second pre-caudal vertebrae for 9 different quantities (A-I). Each point represents a single animal, with the corresponding trait assessed at two resolutions: medium (21μm voxel size) and high (10.5μm voxel size). WT animals (n=3) are depicted as circles and *bmp1a*$^{-/-}$ fish (n=3) as squares. Linear regressions revealed a high level of correlation between phenotypic traits. Further, t-tests showed similar p-values when comparing WT vs *bmp1a*$^{-/-}$ at each resolution.

bioRxiv preprint doi: https://doi.org/10.1101/105569; this version posted March 2, 2017. The copyright holder for this preprint (which was not certified by peer review) is the author/funder. All rights reserved. No reuse allowed without permission.

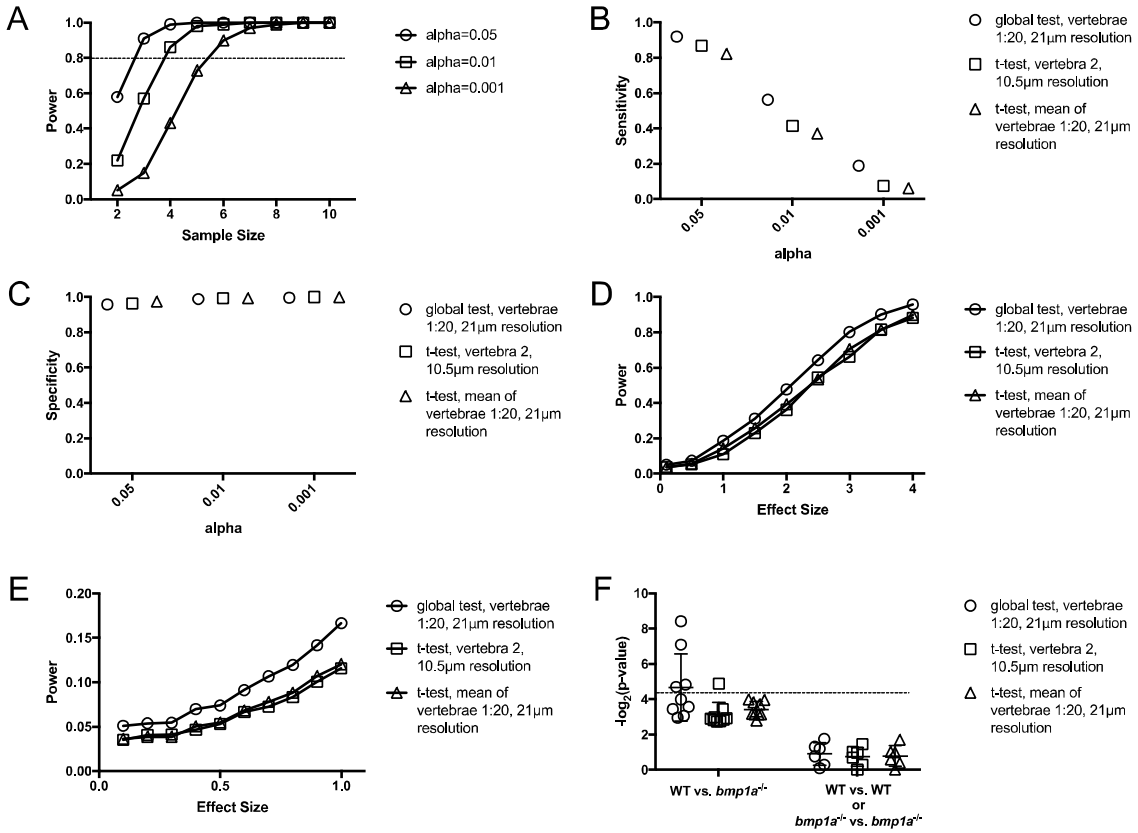

Figure 4. Vertebral patterns, in concert with the global test, confers heightened sensitivity with similar sensitivity in discriminating mutant populations compared to t-tests of individual vertebrae or t-tests of quantities averaged over multiple vertebrae. Figures A-F show results from Monte Carlo simulations. (A) Power of the global test in discriminating differences in Tot.TMD in *bmp1a*$^{-/-}$ and WT fish as a function of sample size and alpha value. The dotted line highlights sample sizes with power >0.8. (B) Sensitivity (fraction of times in which p<0.05 when comparing *bmp1a*$^{-/-}$ vs. WT fish) for different test procedures. (C) Specificity (1 - fraction of times in which p<0.05 when comparing WT vs. WT fish) for different test procedures. (D) Power as a function effect size for different test procedures. (E) Closeup of figure (D) for smaller effect sizes. (F) Comparison of different test procedures using experimental data. Each point in the plot represents the p-value derived from comparisons of four fish (n=2/group) using the groupings listed in Table 1. Points with a value greater than -log2(0.05)=4.32 (denoted by the dotted line) are statistically significant.

bioRxiv preprint doi: https://doi.org/10.1101/105569; this version posted March 2, 2017. The copyright holder for this preprint (which was not certified by peer review) is the author/funder. All rights reserved. No reuse allowed without permission.

bioRxiv preprint doi: https://doi.org/10.1101/105569; this version posted March 2, 2017. The copyright holder for this preprint (which was not certified by peer review) is the author/funder. All rights reserved. No reuse allowed without permission.

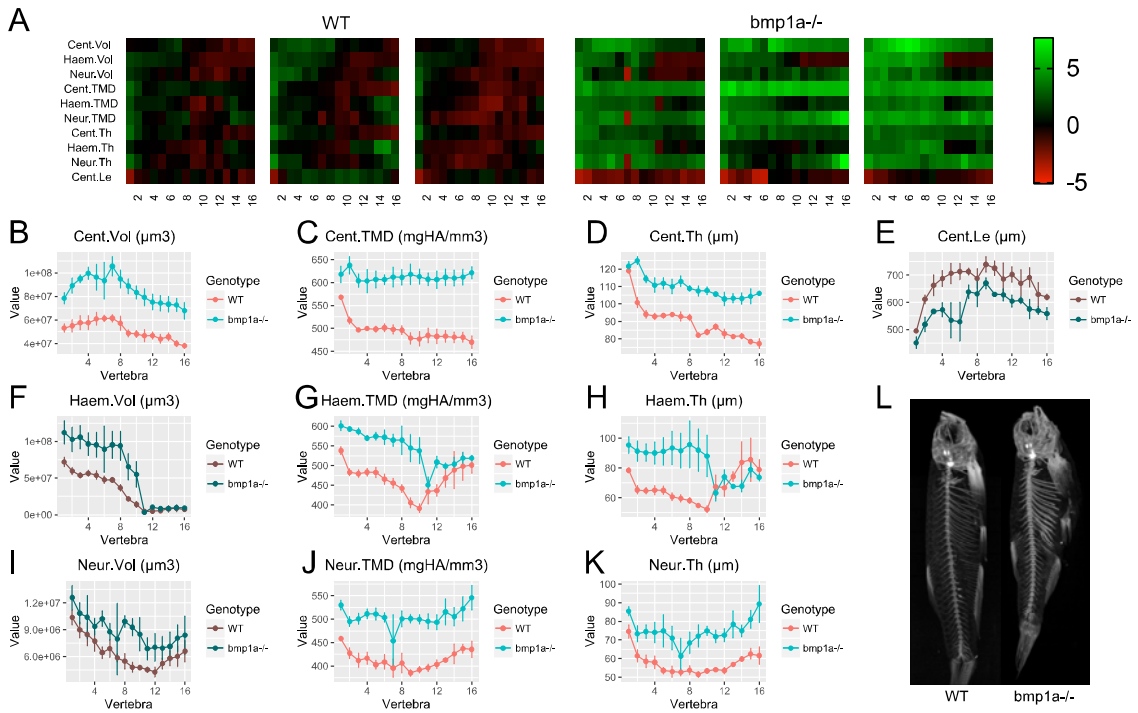

Figure 5. Analysis of *bmp1a*$^{-/-}$ fish. (A) Skeletal barcodes for WT and *bmp1a*$^{-/-}$ fish (n=3/group). Each barcode represents a single fish. Standard scores are computed as the difference between the value of the trait in the individual and the mean value of the trait across all vertebrae in the control population, divided by the standard deviation of the trait across all vertebrae in the control population (see text for details). (B-K) Phenotypic traits plotted as a function of vertebra (mean±SE, n=3/group). Plots associated with a significant difference are colored in a lighter coloring scheme (see text for p-values). (L) Maximum intensity projection of microCT scans.

bioRxiv preprint doi: https://doi.org/10.1101/105569; this version posted March 2, 2017. The copyright holder for this preprint (which was not certified by peer review) is the author/funder. All rights reserved. No reuse allowed without permission.

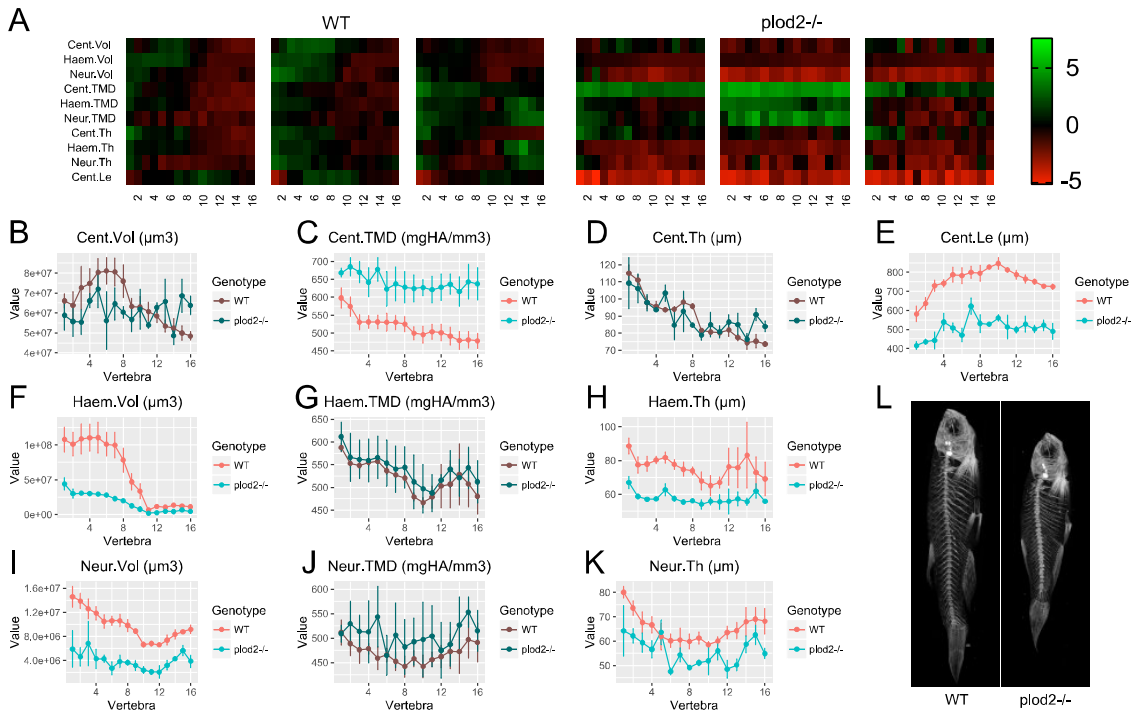

Figure 6. Analysis of *plod2*$^{-/-}$ fish. (A) Skeletal barcodes for WT and *plod2*$^{-/-}$ fish (n=3/group). (B-K) Phenotypic traits plotted as a function of vertebra (mean±SE, n=3/group). Plots associated with a significant difference are colored in a lighter coloring scheme (see text for p-values). (L) Maximum intensity projection of microCT scans.

bioRxiv preprint doi: https://doi.org/10.1101/105569; this version posted March 2, 2017. The copyright holder for this preprint (which was not certified by peer review) is the author/funder. All rights reserved. No reuse allowed without permission.

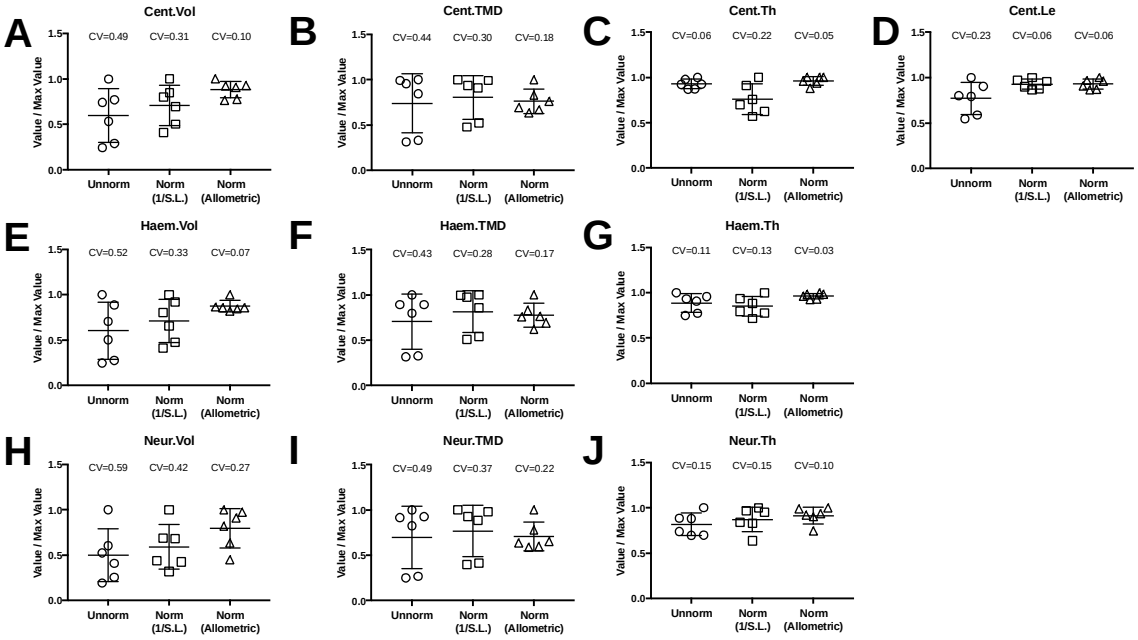

Figure 7. Allometric models reduce phenotypic variability associated with differences in body size. Data are shown for the first precaudal vertebra of WT fish of different standard lengths. The left column shows high phenotypic variability in unnormalized data. When data were normalized using allometric models (right column), phenotypic variability was substantially reduced. Phenotypic variability was also reduced, though to a lesser extent, when data were normalized using an alternate normalization, 1/S.L. (middle column).

bioRxiv preprint doi: https://doi.org/10.1101/105569; this version posted March 2, 2017. The copyright holder for this preprint (which was not certified by peer review) is the author/funder. All rights reserved. No reuse allowed without permission.

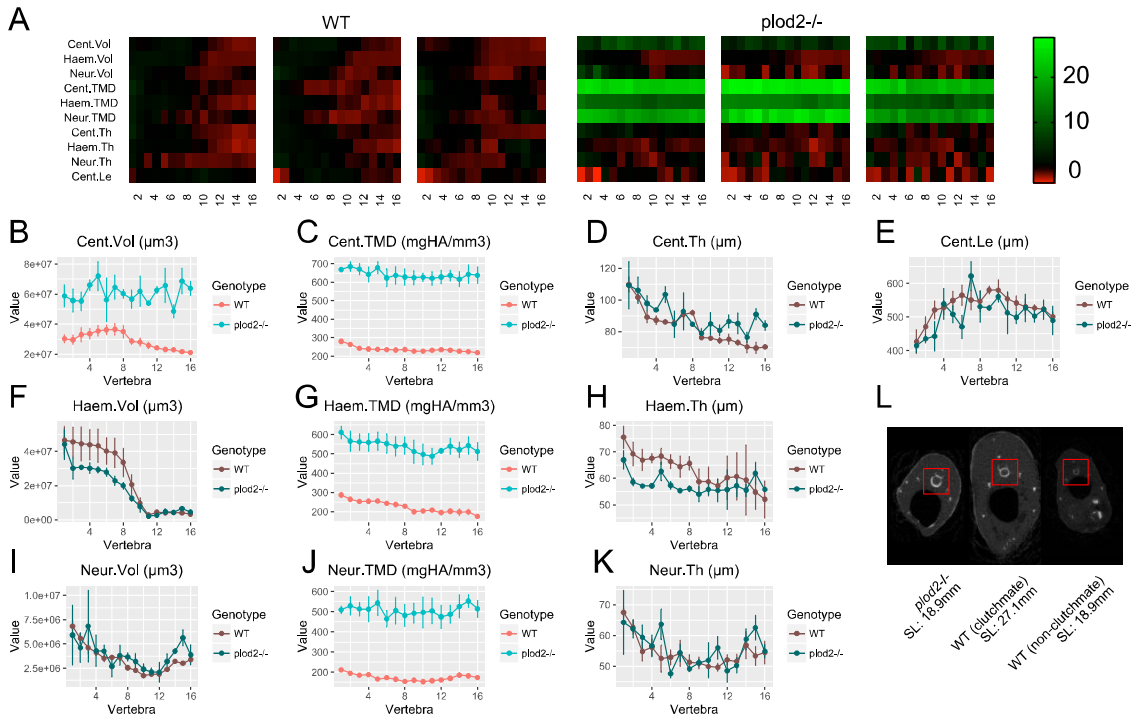

Figure 8. Analysis of *plod2*$^{-/-}$ fish following removal of allometric effects of body size. (A) Skeletal barcodes for WT and *plod2*$^{-/-}$ fish following removal of allometric effects of body size (n=3/group). (B-K) Phenotypic traits as a function of vertebra (mean±SE, n=3/group). Phenotypic data in WT sibling controls were scaled by allometric normalization; data in *plod2*$^{-/-}$ fish are identical to those in Figure 5. Plots associated with a significant difference are colored in a lighter coloring scheme (see text for p-values). (K) Transverse sections of microCT scans. Centra are highlighted by a red box in each animal. *plod2*$^{-/-}$ mutants (left) exhibit increased centrum diameter compared to standard length-matched, non-clucthmate WT controls (right), and to a lesser extent, WT siblings (middle) of greater standard length. Images show posterior endplate of the sixth precaudal vertebra in all fish.

bioRxiv preprint doi: https://doi.org/10.1101/105569; this version posted March 2, 2017. The copyright holder for this preprint (which was not certified by peer review) is the author/funder. All rights reserved. No reuse allowed without permission.

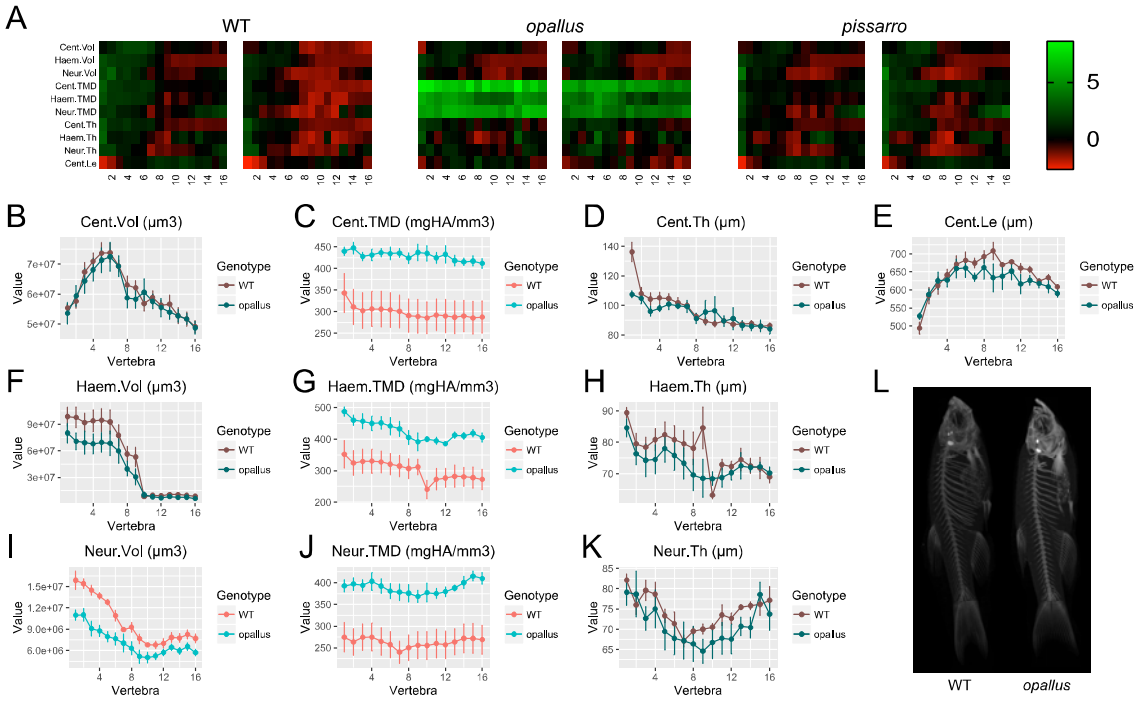

Figure 9. Identification of *opallus* as a novel axial skeletal mutant. (A) Skeletal barcodes for WT, *opallus*, and *pissarro* (n=2 fish/group). Barcodes for *opallus*, but not *pissarro*, appear different from WT fish (B-K) Phenotypic traits in *opallus* plotted as a function of vertebra (mean±SE, n=5/group). Plots associated with a significant difference are colored in a lighter coloring scheme (see text for p-values). (L) Maximum intensity projections of microCT scans.

bioRxiv preprint doi: https://doi.org/10.1101/105569; this version posted March 2, 2017. The copyright holder for this preprint (which was not certified by peer review) is the author/funder. All rights reserved. No reuse allowed without permission.

TABLE LEGENDS

Vert	Cent.Vol	Haem.Vol	Neur.Vol	Cent.TMC	Haem.TMC	Neur.TMC	Cent.Th	HaemTh	Neur.Th	Cent.Le
1	2.44	2.63	2.34	4.79	4.85	5.07	0.15	0.50	0.53	0.96
2	2.38	2.50	2.82	4.79	4.78	5.65	0.28	0.35	0.50	0.94
3	2.44	2.81	3.13	4.87	5.20	6.04	0.29	0.47	0.65	1.05
4	2.48	2.89	3.25	4.96	5.31	6.13	0.28	0.53	0.53	1.06
5	2.54	2.95	3.37	5.05	5.37	6.51	0.26	0.55	0.51	1.11
6	2.50	2.90	3.33	5.02	5.34	6.41	0.30	0.49	0.40	1.01
7	2.46	2.94	3.35	5.00	5.42	6.46	0.24	0.46	0.34	1.16
8	2.41	2.67	4.18	4.89	5.21	7.43	0.12	0.36	0.48	1.16
9	2.46	2.61	4.20	4.91	5.32	7.44	0.21	0.45	0.57	1.10
10	2.52	3.94	4.16	4.93	6.50	7.43	0.19	0.32	0.49	1.17
11	2.64	2.79	3.99	5.04	5.36	7.27	0.24	0.49	0.59	1.19
12	2.72	2.96	3.89	5.07	5.86	7.12	0.27	0.72	0.62	1.16
13	2.57	3.03	3.48	4.89	5.85	6.64	0.18	0.68	0.68	1.14
14	2.55	3.59	2.94	4.86	6.61	5.82	0.18	1.03	0.55	1.10
15	2.57	3.49	3.32	4.93	6.37	6.41	0.24	0.87	0.80	1.02
16	2.57	3.79	3.06	4.98	6.89	6.26	0.14	0.87	0.69	1.15

Table 1. Scaling exponents (i.e., values of b) computed in allometric models. Expected values for isometric scaling with standard length are as follows: Vol: b=3, TMC: b=3, Th: b=1, Le: b=1

bioRxiv preprint doi: https://doi.org/10.1101/105569; this version posted March 2, 2017. The copyright holder for this preprint (which was not certified by peer review) is the author/funder. All rights reserved. No reuse allowed without permission.

SUPPLEMENTARY FIGURE LEGENDS

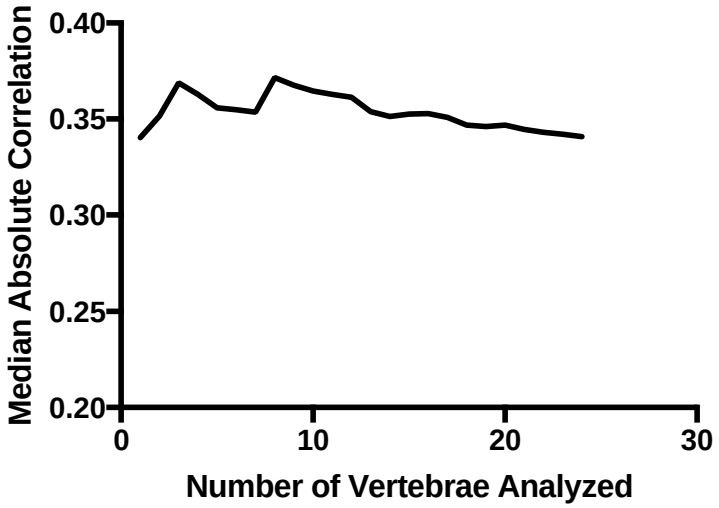

Fig 2-Figure Supplement 1. Median absolute correlation plotted as a function of number of vertebrae analyzed. The median absolute correlation was relatively invariant with increasing number of vertebrae used for analysis, suggesting that each vertebrae confers non-redundant information.

bioRxiv preprint doi: https://doi.org/10.1101/105569; this version posted March 2, 2017. The copyright holder for this preprint (which was not certified by peer review) is the author/funder. All rights reserved. No reuse allowed without permission.

Comparison	Group 1	Group 2
WT vs. mutant	WT1, WT2	mutant1, mutant2
	WT1, WT2	mutant1, mutant3
	WT1, WT2	mutant2, mutant3
	WT1, WT3	mutant1, mutant2
	WT1, WT3	mutant1, mutant3
	WT1, WT3	mutant2, mutant3
	WT2, WT3	mutant1, mutant2
	WT2, WT3	mutant1, mutant3
	WT2, WT3	mutant2, mutant 3
WT vs. WT	WT1, WT2	WT1, WT3
	WT1, WT2	WT2, WT3
	WT1, WT3	WT2, WT3
mutant vs. mutant	mutant1, mutant2	mutant1, mutant3
	mutant1, mutant2	mutant2, mutant3
	mutant1, mutant3	mutant2, mutant3

Fig 4-Figure Supplement 1. Experimental groups used for sensitivity analysis.

bioRxiv preprint doi: https://doi.org/10.1101/105569; this version posted March 2, 2017. The copyright holder for this preprint (which was not certified by peer review) is the author/funder. All rights reserved. No reuse allowed without permission.

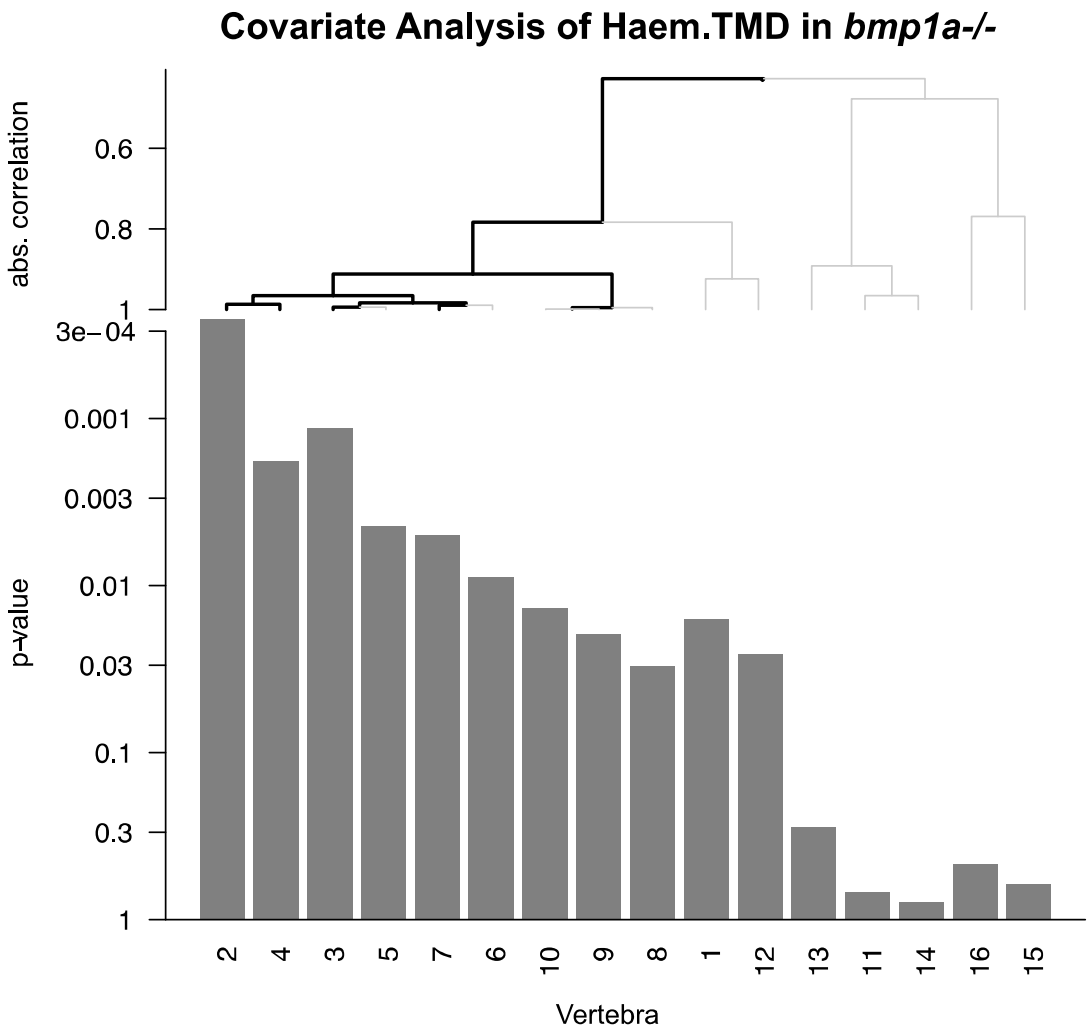

Fig 5-Figure Supplement 1. Covariate analysis of Haem.TMD in *bmp1a*$^{-/-}$ fish. Vertebrae were hierarchically clustered based on association with mutation, and a multiplicity-corrected procedure was used to identify portions of the graph that exhibit a significant association with mutation (highlighted in black). Significant associations are observed for vertebrae 2, 3, 4, and 7. Note that for vertebrae 9/10 significant branches did not reach all the way to the "leaf nodes"; in this case, we are able to infer that at least one of the vertebrae 9 or 10 was significantly associated with genotype, but not which one.

bioRxiv preprint doi: https://doi.org/10.1101/105569; this version posted March 2, 2017. The copyright holder for this preprint (which was not certified by peer review) is the author/funder. All rights reserved. No reuse allowed without permission.

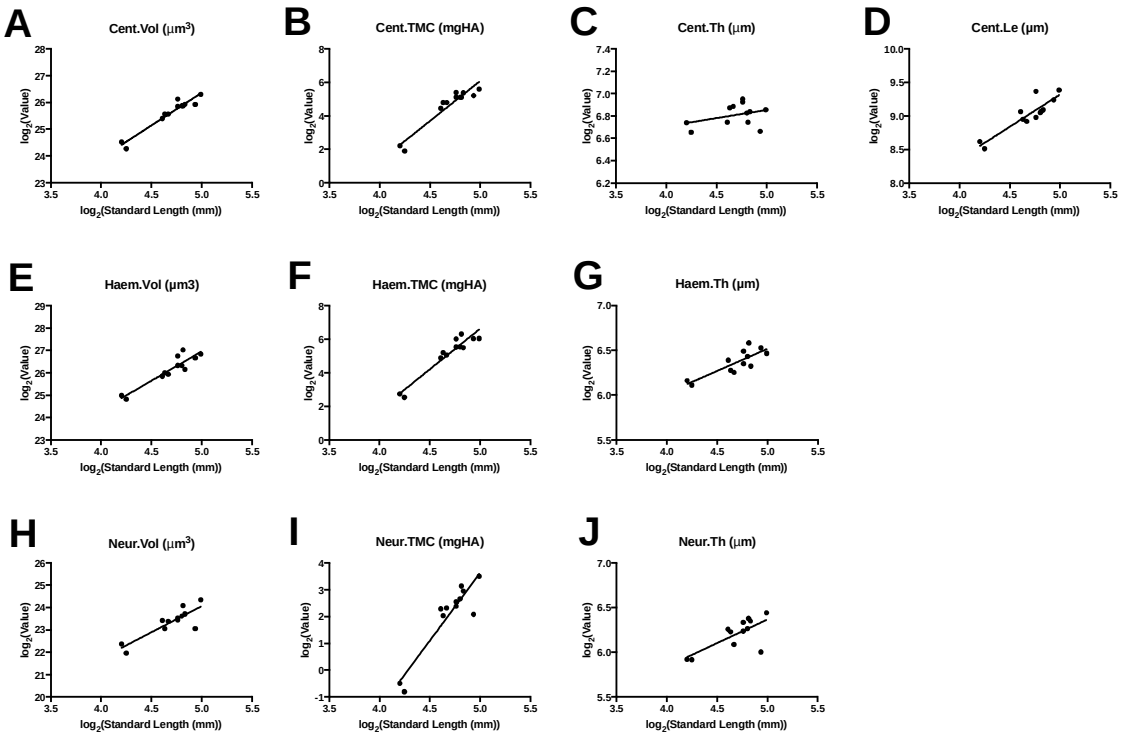

Figure 7-Figure Supplement 1. Allometric modeling of phenotypic traits. Phenotypic traits plotted as a function of standard length. Linear fits of log-transformed data were used to compute allometric model parameters. Data are shown for the first precaudal vertebra.

bioRxiv preprint doi: https://doi.org/10.1101/105569; this version posted March 2, 2017. The copyright holder for this preprint (which was not certified by peer review) is the author/funder. All rights reserved. No reuse allowed without permission.

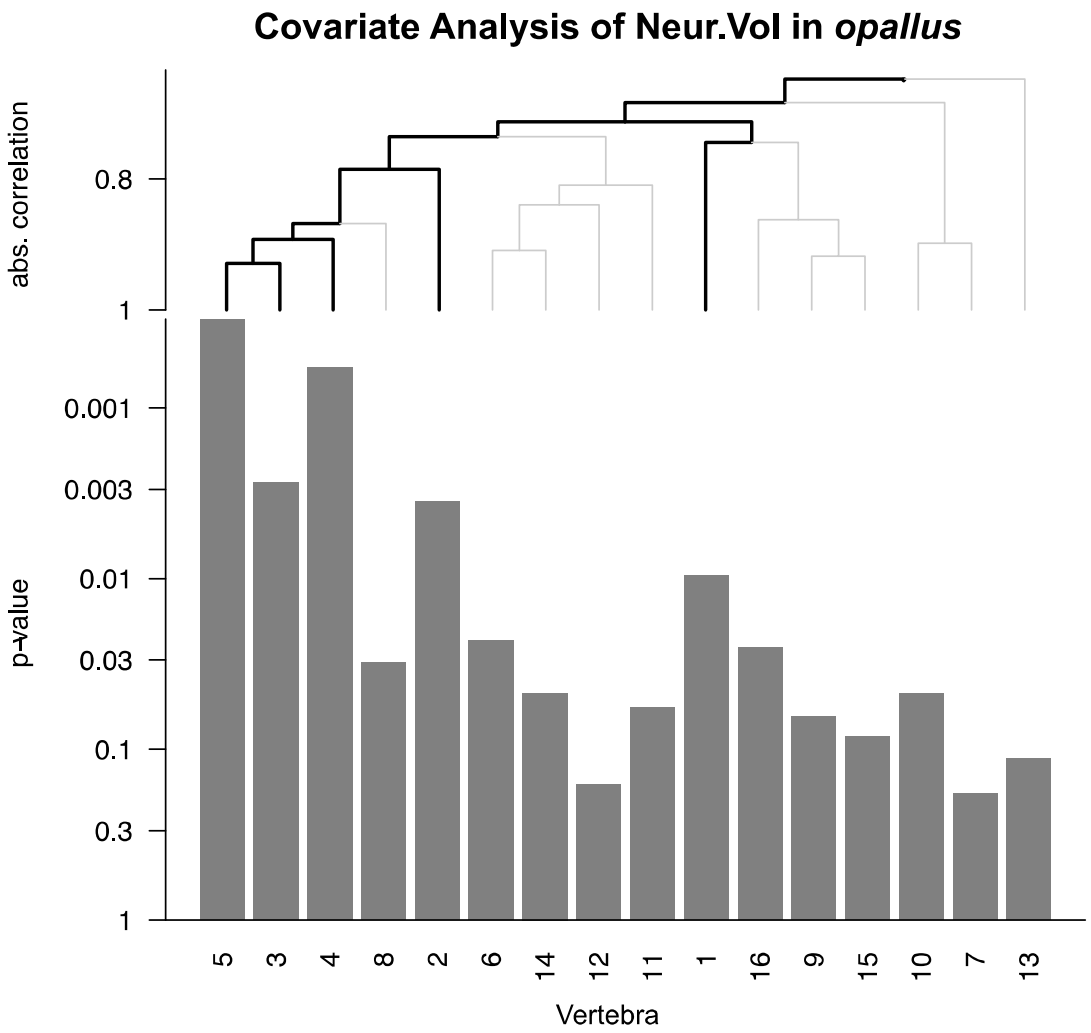

Figure 9-Figure Supplement 1. Covariate analysis of Neur.Vol in *opallus*. See Fig S2 for interpretation of graph. Significant associations are observed for vertebrae 1-5 only.

bioRxiv preprint doi: https://doi.org/10.1101/105569; this version posted March 2, 2017. The copyright holder for this preprint (which was not certified by peer review) is the author/funder. All rights reserved. No reuse allowed without permission.

SOURCE DATA LEGENDS

Figure 2-Source Data 1. Zip file containing phenotypic data (one text file per fish) as well as R code used for analysis.

Figure 3-Source Data 1. Zip file containing phenotypic data (one text file per fish) as well as R code used for analysis.

Figure 4-Source Data 1. Zip file containing phenotypic data (one text file per fish) as well as R code used for analysis.

Figure 5-Source Data 1. Zip file containing phenotypic data (one text file per fish) as well as R code used for analysis.

Figure 6-Source Data 1. Zip file containing phenotypic data (one text file per fish) as well as R code used for analysis.

Figure 7-Source Data 1. Zip file containing phenotypic data (one text file per fish) as well as R code used for analysis.

Figure 8-Source Data 1. Zip file containing phenotypic data (one text file per fish) as well as R code used for analysis.

Figure 9-Source Data 1. Zip file containing phenotypic data (one text file per fish) as well as R code used for analysis.

bioRxiv preprint doi: https://doi.org/10.1101/105569; this version posted March 2, 2017. The copyright holder for this preprint (which was not certified by peer review) is the author/funder. All rights reserved. No reuse allowed without permission.